13th ewtec 2019 Proceedings of the 13th European Wave and Tidal Energy Conference 1-6 Sept 2019, Naples, Italy

Hydrodynamic modelling of flexible tidal turbine blades

Federico Zilic de Arcos, Christopher Vogel, Richard H. J. Willden

Abstract—**The current work is an analysis of the hydrodynamic effects of the different deformation mechanisms that affect axial-flow tidal turbines with the intention of understanding to what extent hydroelastic effects could be employed to improve the performance or to reduce the loads in rotors. For that, a simple hydroelastic model is employed to obtain the deformed geometries of a turbine, which are then de-coupled into edgewise, flapwise, and twist deformations.**

The deformation data is used to analyse, by the means of blade-resolved CFD simulations, four different cases, for which the rotor geometries were rebuilt: The originally designed rotor simulated as if it was a rigid structure; the blade with just flapwise deformation, retaining the original twist angles; only the twist deformation and; finally, the deformed rotor with all the deformation components, as obtained from the hydroelastic model. For each case, three different tip-speed ratios were analysed (4.0, 5.5 and 7.0) at a flow speed of 4.5 [m/s]. It is from these simulations that the influence of the different deformation mechanisms is quantified, as well as the relative independence and interaction of the hydrodynamic phenomena associated with them.

Keywords—**Tidal turbines, energy, fluid-structure interaction, hydroelasticity, rotor design, deformation.**

I. Introduction

TIDAL streams are a promising energy source as they are a renewable and predictable resource. Deriving from experience in the wind industry, the majority tidal stream turbine designs are of the axialflow turbine type (e.g. MCT SeaGen S, Hydro Hammerfest HS1000, Voith Hydro). Although these devices are conceptually similar to the rotors used to extract energy from the wind, there are important differences in terms of the environmental, flow conditions and operational constraints that affect the behaviour and the operating conditions of these turbines. In particular, the higher fluid density and the effect of flow confinement due to the proximity of the seabed, sea surface, and potentially neighbouring turbines, may all lead to significant loading on tidal turbine blades. Furthermore, challenges in access and maintenance in the marine environment mean that mechanically complex systems, such as active pitch-to-feather rotor control which is widely used by wind turbines to limit extreme loadings [1], may not be as effective from a whole-system perspective for tidal stream turbines.

This results in high uncertainty in the engineering of cost-effective turbines for tidal streams, as the load-cases for structural design are not thoroughly understood nor defined, leading to over conservative approaches or premature failure. For this reason, the present work intends to explore the hydrodynamic effects associated with the different deformation mechanisms that blades may experience in order to investigate the potential for passive control strategies based on hydroelastic phenomena.

The deformation of a rotor blade can be understood as a combination of three main mechanisms: Flapwise deformation, driven by thrust forces; edgewise deformation, driven by the tangential forces and typically small compared to flapwise deformations; and twist deformation caused by the sectional pressure distribution and by the interaction between the loads and the structural response of the blade [2], altering the twist distribution over the span of the blade. These different mechanisms can be seen in the schematic shown in Fig. 1.

The concept of using fluid-structure interaction phenomena in rotor designs is not new, and is supported by the fact that the deformations seen in tidal and wind rotors tend to be significant. For example, Nicholls-Lee et.al. (2011) described a 20m diameter tidal rotor that exhibited 1.48m of flapwise displacement [3] ; Grogan et.al. (2013) designed a 12m length tidal turbine blade for a 1.5MW rated rotor, showing deformations from 1.75m to 4.10m depending on the material selection [4]; and Rafiee et al. (2016) reported a maximum deformation of 1.46m for a 47m diameter wind turbine[5],showing a much stiffer behaviour than the previous cases.

Studies have been performed on the fluid-structure interaction phenomena of tidal turbines. Some used a 1-way approach (e.g. Bir et al.(2011) [6], Grogan et al. (2013)

Paper ID number: 1587; Conference track: Tidal hydrodynamic modelling.

This work was supported in part by CONICYT PFCHA/BECAS CHILE DOCTORADO EN EL EXTRANJERO 2016 /72170292.

F. Zilic de Arcos*, C. Vogel and R.H.J. Willden are with Department of Engineering Science, University of Oxford, Parks Road, OX1 3PJ, UK.

*Corresponding author: federico.zilic@eng.ox.ac.uk

[4], Wang (2016) [7]) in which hydrodynamic loads are applied to a structural model to obtain the resulting blade deformations.

This work focusses on coupled hydrodynamic and structural analysis (2-way method) where an iterative solution is employed to link the hydrodynamic loads and the resulting blade deformations, which in turn modify the hydrodynamic loads.

Examples of this kind of approach are the works of Nicholls-Lee and Nicholls-Lee et al., that demonstrate a method to design and optimise composite-laminated rotor blades, in which a Finite Elements solver (FEM) was coupled with a surface panel code to generate the hydrodynamic loads, to obtain a steady-state solution and optimised turbine structure [3], [8]. Murray et.al. (2016) designed a tidal rotor using the Blade Element Momentum (BEM) and a FEM solver. X-Foil was used to calculate the lift and drag coefficients, neglecting the moment coefficients [9] and obtained a relatively good agreement with experimental results [10].

Similar studies have been undertaken for wind turbines: Bazilevs et al.(2011) developed a strongly coupled model based on transient CFD simulations and a shell-based structural model, showing good agreement with published results for a 5MW rotor [11]. Wang et al. (2014) developed a nonlinear aerolastic model for a 1.5MW wind turbine based on one-dimensional geometrically exact beam theory coupled with a BEM code [12]. Rafiee et al. (2016) coupled a commercial shell-based finite elements software with a BEM code, showing diminished performance for an elastic 660kW rotor compared to the rigid counterpart [5].

2-way methods are particularly important when studying the performance of rotors when the blade deformations are large enough to influence the hydrodynamic behaviour. However, still the underlying physics of the phenomena are not thoroughly understood, leading to difficulties when defining which models are appropriate for different applications.

This paper is focused on describing the hydrodynamic effects that result as aconsequence of a blade deformation by decoupling the deformation mechanisms of a rotor and focusing mainly on the flapwise and twist-wise deformations. A rotor designed by Schluntz and Willden (2015) [13] and subsequently modified by Wimshurst and Willden [14] was employed. The blade design (both structural and hydrodynamic) are briefly presented in the sub-section III-A.

The deformations were obtained from an engineering BEM-based hydroelastic model, briefly introduced in section II, at three different Tip-Speed Ratios (4.0, 5.5 and 7.0) and a constant flow-speed of 4.5m/s. The deformations were decoupled in flapwise, edgewise and twist, as presented in section III.

The geometries of four different cases (rigid, only flapwise deformation, only twist, and the fully deformed blade) were constructed on a CAD software and analysed using blade-resolved steady-state RANS CFD simulations, reproducing the conditions of the hydroelastic model. The results from this process were used to measure the influence of the different deformation mechanisms in terms of the integrated quantities (power and thrust coefficients), the spanwise force distributions and the axial induction factors.

Fig. 1. Diagram of the different deformation mechanisms as seen from side and top views.

II. HYDROELASTIC MODEL

An engineering hydroelastic model based on the Blade Element Momentum theory and a shell-based finite elements solver was employed to obtain the deformations of the blade at different operational conditions under steady flow assumptions.

The hydroelastic solver reproduces blade loads as a three-dimensional field, reproducing the sectional pressure distributions and thus the moments as well. These fields are then interpolated over the surface elements of the structural solver, from which the angular deformations are re-imposed in the hydrodynamic solver, iterating until thrust and power convergence are achieved. This model neglects the influence of the flapwise deformation component, assuming it to negligible compared the hydrodynamic effects of the twist-wise deformations.

For hydrodynamic modelling, the model uses the BEM implementation described by Ning (2014) [15], the empirical model for the turbulent wake region described by Buhl (2005) [16] and a Prandtl tip-loss correction factor [1]. This particular implementation of the BEM theory uses the traditional derivation where the conservation of momentum and blade element equations are solved, but describes the system of equations in terms of the inflow

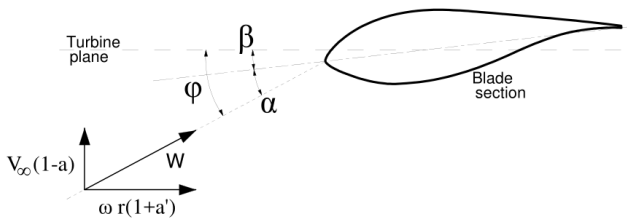

Fig. 2. Flow diagram over an arbitrary section of the blade, as described by the BEM theory.

angle ϕ (see fig. 2), reducing the problem to find the solution of a single residual equation $H(\phi)$ (eq. 1), where a is the axial induction factor, a' the tangential induction factor and λ_r is the local tip-speed ratio:

$$H(\phi) = \frac{\sin(\phi)}{1-a} - \frac{\cos(\phi)}{\lambda_r(1+a')} = 0 \tag{1}$$

The full discussion of this implementation falls beyond the scope of this paper, but the entire derivation and a mathematical proof of the existence of a solution to the system of equations can be found in the original reference [15].

The blade loads are reproduced in the structural model as three-dimensional pressure fields using two-dimensional hydrofoil coefficients derived from CFD simulations, and applied to the different blade sections as a function of the position $\vec{X}$; the local inflow velocity (W) and the angle of attack α as obtained from the BEM:

$$C_{pres} = f(\vec{X}, \alpha) \tag{2}$$

$$p = \frac{1}{2}\rho W^2 C_{pres} + p_0 \tag{3}$$

where p_0 is the static pressure component, ρ the fluid density and C_{pres} are the two-dimensional pressure coefficients obtained from 2D CFD simulations(calculated for a wide range of angles *a priori*), expressed as a function of the angle of attack. This results in a 3D field of pressures re-evaluated at each iteration.

For the structural model, the commercial solver ANSYS Mechanical 18.1 was employed. SHELL181 elements were selected as they can predict the behaviour of moderately-thick multi-layered structures, such as the ones used for composite turbine blades. The structural design utilised here was described in Zilic de Arcos et al. (2018) [17] with reduced flexibility.

Further details about the model, including a more extensive description of the solver components and the structural design can be found in [17].

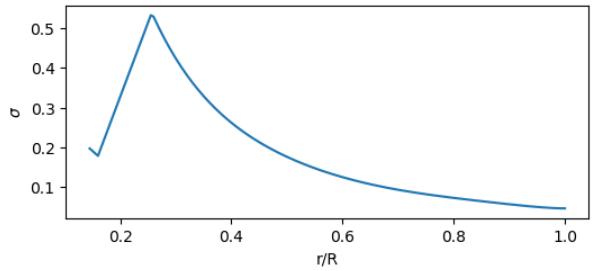

(a) Blade solidity

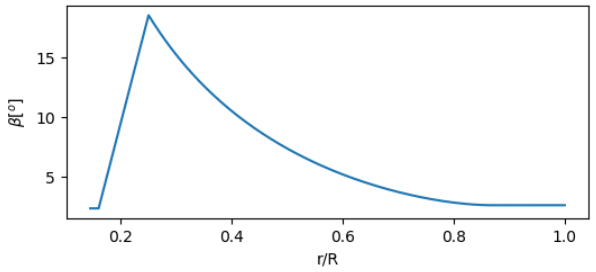

(b) Blade twist angle

Fig. 3. Original rotor geometric characteristics as functions of the radial position [14].

III. ROTOR DEFORMATION CASES

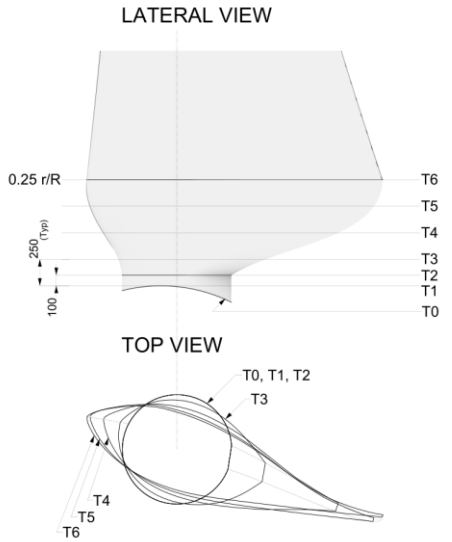

Fig. 4. Details of the modified blade root section. The lateral and top views display the soft transition between the blade and the nacelle. Dimensions are in millimetres.

A. *Base rotor design*

The rotor employed in this paper is a hydrodynamic design developed by Schluntz and Willden (2015) [13] for a blocked flow condition, under a ratio of the rotor to channel areas of 0.197; and further modified by Wimshurst and Willden (2016) [14] in its root section.

The rotor uses the RISØA1-24 aerofoil centered at 25% of the chord. The twist angle β and the solidity $\sigma = cB/(2\pi r)$, where c is the sectional chord, B the number of

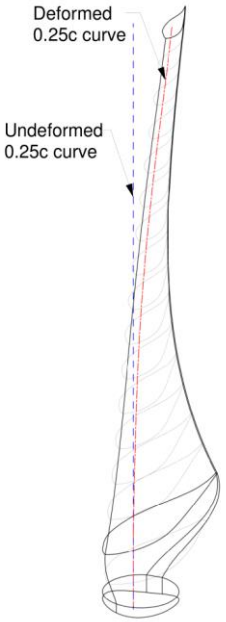

Fig. 5. Curvature of the quarter-chord line of the deformed and undeformed cases.

blades and r the local radius, can be seen in figures 3 (a) and (b), respectively.

Although the original blade twist and solidity profiles were maintained outboard of $r = 0.25R$, where r is the radial position and R is the turbine radius, the transition geometry from the nacelle up to $r = 0.25R$ was modified to obtain a better surface continuity with the blade rest of the blade to ensure a better stress transition between the two regions. The detailed modification is shown in Fig. 4.

B. Deformed cases

In this work, the deformations are assumed to be a combination of different mechanisms that can be linearly super-imposed to obtain the fully-deformed case. These mechanisms are the flapwise, edgewise and twist deformations. It is assumed that the blade only exhibits beam-like deformation, neglecting any changes in the transverse aerofoil sections.

The frame of reference to track the deformations is based on the quarter-chord line ($0.25c$). This is an imaginary segment around which the aerofoil sections are centered in the rotor design, and that for the original design (undeformed) is a straight segment with coordinates $f(X,Y,Z) = (0,0,r)$, where X is the thrustforce direction (in the direction of the undisturbed flow velocity), Y the tangential-force direction, Z the spanwise coordinate and r the local coordinate for the different radial stations. This is shown in Fig. 5.

The flapwise and edgewise deformations deflect the quarter-chord line, whereas twist deformations change the twist angle without changing it.

1) *Deformations of the quarter-chord line:* The flapwise and edgewise deformations were obtained by tracking, from the Finite Elements solution of the converged hydroelastic

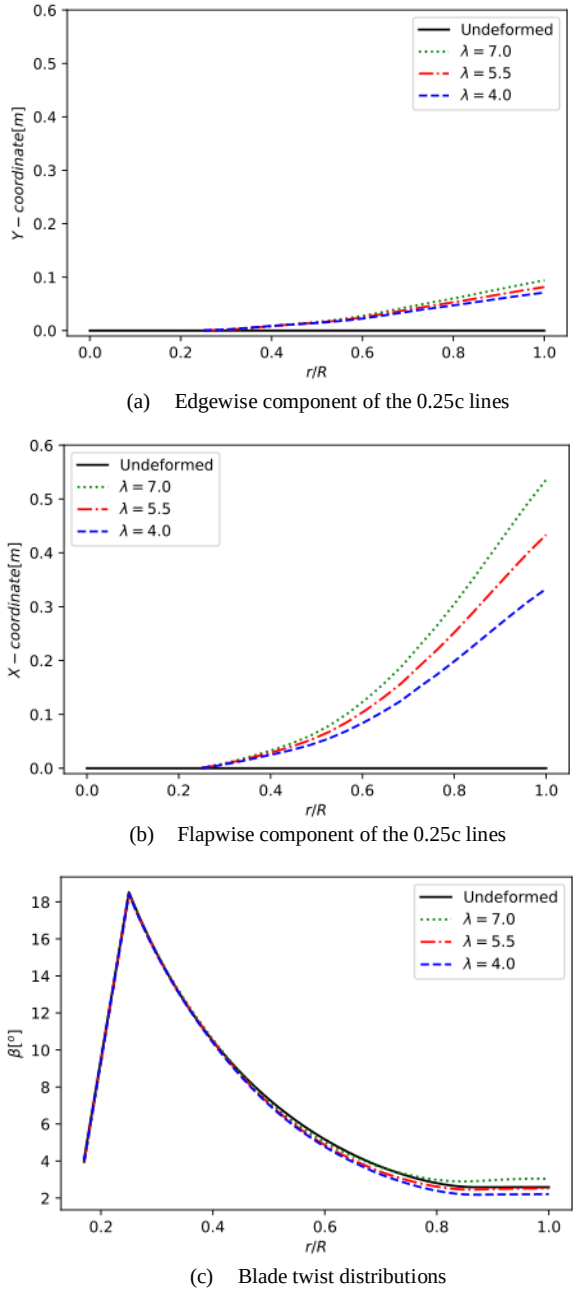

(a) Edgewise component of the 0.25c lines

(b) Flapwise component of the 0.25c lines

(c) Blade twist distributions

Fig. 6. Comparison of blade quarter-chord lines (a and b) and the twist distributions(c) for the rigid and the deformed cases at a flow-speed of 4.5 m/s and tip-speed ratios of 4.0, 5.5 and 7.0.

model, the change of position of the 0.25c line, from the root to the tip of the rotor.

In Figs. 6, plots of the deformations of the 0.25c lines can be seen for the different analysed tip-speed ratios. The deformed curves were used to define translations of the foil sections, although the twist angles were preserved, as shown in Fig. 5.

To rebuild the geometries of these cases and to set up the CFD model, only the flapwise component (X-coordinate) of the deformation was taken into account, neglecting the edgewise displacement (See Figs. 6 (a) and (b)).

2) *Twist-only deformation*: The twist deformations were also obtained, as in the previous section, from the Finite Elements resultsafter convergence of the hydroelastic

model. A set of nodes over the blade span were tracked and their relative angular positions compared to the original model, obtaining the twist deformations as a function of the radial position.

These angular differences were added to the original twist angle of the blade, to obtain the modified twist distributions seen in Fig. 6 (c). These were used to rebuild the rotor geometry maintaining the corresponding quarter-chord line.

From the Fig. 6 (c) it can be seen that the angular differences are relatively small. However, rotor performance is sensitive to the optimal angle of attack for maximising the lift-to-drag ratio [18]. Consequently, small changes in angle of attack can lead to significant changes in performance.

3) *Fully-deformed blade*: The fully deformed case was generated using all three deformation components in the hydroelastic model

IV. CFD Simulations

C. Numerical methods

Reynolds-Averaged Navier Stokes(RANS) CFD simulations were employed with a cell-centered finite volumes discretization, a second-order upwind spatial discretization scheme and a coupled-pressure algorithm, with the latter meant to provide more robustness and efficiency in single phase flows under steady-state conditions [19].

High-fidelity rigid structured meshes were employed to model the turbines, ensuring that the elements around the rotor maintained a high quality. This approach was selected instead of more complex methods, such as transient fluid-structure interaction simulations with an immersed body or morphing mesh that could reduce overall accuracy.

The commercial software Fluent 19.0 was used to solve RANS equations. The $k-\omega$ SST turbulence model [20] with updated constants [21] was employed with an enhanced wall-modelling approach [19]. This represents a method widely employed to reproduce the flow behaviour and the performance of wind and tidal rotors.

The control volume was modelled using a cylindrical domain, exploiting the axisymmetry of the problem to only model a 120 degrees wedge using non-conformal interfaces and periodic boundary conditions.

The outer diameter of the domain was 5.0 times that of the rotor in order to minimise any blockage-related effects [22]; the length of the cylinder, upstream the turbine plane, was 5 times the rotor radius, whereas the length downstream was set as 14 times the rotor radius, in order to provide sufficient distance for flow development without the boundaries significantly influencing the flow behaviour.

The blade rotation was modelled using the Moving Reference Frame approach (MRF) [23]. This method works by having multiple subdomains in which different

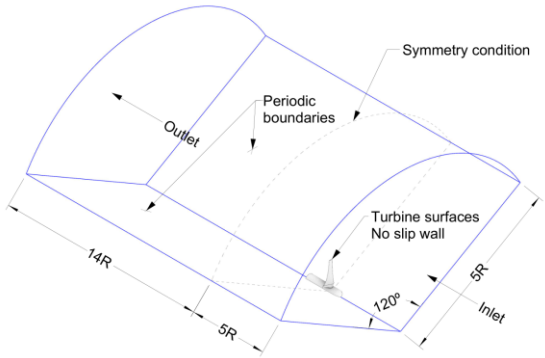

Fig. 7. Diagram of the CFD domain. Note that the drawing is not to scale.

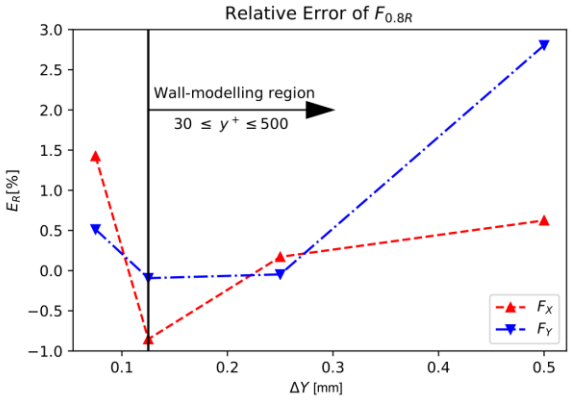

Fig. 8. Relative error for the different first element thickness values. Notice the increasing error in (a) thrust and (b) the tangential force at $0.8R$ when $\Delta Y < 0.125$ $[mm]$: It is caused by the model entering a buffer region where $5 < Y^+ < 30$. In this region, the wall-modelling approach is no longer valid, but the mesh is still too coarse to resolve the boundary layer.

rotational speeds can be applied using the moving reference frame equations, and performing local reference frame transformations at the interfaces to enable the transport of fluxes from one to another. This method allows to model a transient rotational problem as a steady-state case, drastically reducing the computational power requirements.

The solver iterated a minimum of 20,000 times to obtain a solution, running over 64 cores using the Advanced Research Computing facilities of the University of Oxford. During those iterations, the scaled residuals were reduced at least 6 orders of magnitude for continuity and the velocity components, and typically 5 orders for the turbulence constants.

The different boundaries, as seen in the Fig. 7, can be summarised as follows: At the inlet, a uniform velocity of 4.5 m/s was applied, with a turbulence intensity of 10 % and a length scale of 0.7 times rotor diameter of 20m, following the work previously done by Wimshurst and Willden (2015) [14]. All the rotor surfaces were defined as no-slip smooth walls. The outlet was defined by a constant-pressure equal to that of the undisturbed flow, and the outer-cylinder surface was defined with a symmetry condition. Finally, the rotational symmetry of the problem was exploited by defining the wedge sides as

non-conformal periodic boundary conditions, as shown in the corresponding diagram.

D. Meshing details

Structured meshes were employed to perform the simulations presented herein. The initial mesh configuration used 104 elements on the chordwise direction and 140 elements in the spanwise direction, as it was shown in [14] that those values would yield mesh-independent power and thrust coefficients, as well as tangential and thrust forces distribution for this particular rotor. The meshes were generated using ICEM 19.0, with a Y-Mesh topology for the rotatory domain and an O-grid mesh around the blade.

The original mesh sensitivity study was expanded by analysing in more detail the O-Grid region surrounding the blade surfaces, for which three parameters were studied: the number of elements, the growth rate and the first layer thickness.

From the sensitivity analysis, was noticed that the mesh seems to be invariant to the changes in the growth rate and the number of elements. However, there is some degree of sensitivity to the thickness of the first element, for which significant variations at both ends of the analysed range can be seen. This quantity is directly linked with the dimensionless wall distance $Y+ = \Delta Y\, u_\tau/\nu$, with $u_\tau = \sqrt{\tau_W/\rho}$, τ_W the shear stress on the wall and ρ the fluid density; ΔY the normal distance to the wall boundary and ν the kinematic viscosity.

Fig. 8 shows partial results of the sensitivity study, showing the variation in error in thrust and tangential force predictions for different thicknesses of the wall-adjacent cell at 80% of the span. Model convergence is approached as ΔY is reduced, although at a critical $\Delta Y \approx 0.00012\ [m]$, the model enters the buffer region $5 < \Delta Y < 30$. In this range, the model fails because it is not capable of resolving the wall (for which Y^+ should be smaller than 1) nor employing a wall modelling approach, for which Y^+ is expected to be larger than 30.

The meshes in this work used a ΔY of $0.00025\ [m]$ over the blade surfaces, with a growth rate away from the wall of 1.05 and 25 elements in this region. The rest of the regions were adjusted to have a smooth transition with the O-grid, leading to a final count of approximately 4.5 million nodes.

V. RESULTS

E. Integrated thrust and power

The integrated quantities are plotted in the form of non-dimensional power and thrust coefficients. These are defined in equations 4 and 5:

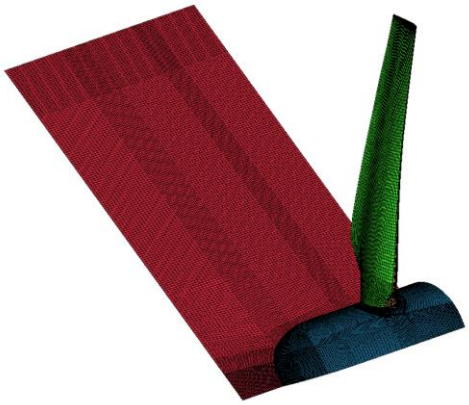

Fig. 9. Mesh of the rotor used for the CFD computations. Flap-only case at $\lambda = 7.0$.

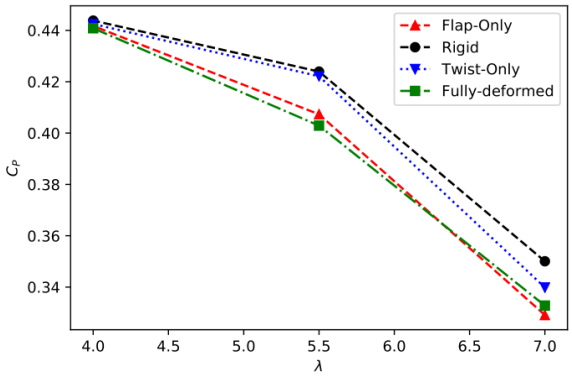

(a) Power coefficients

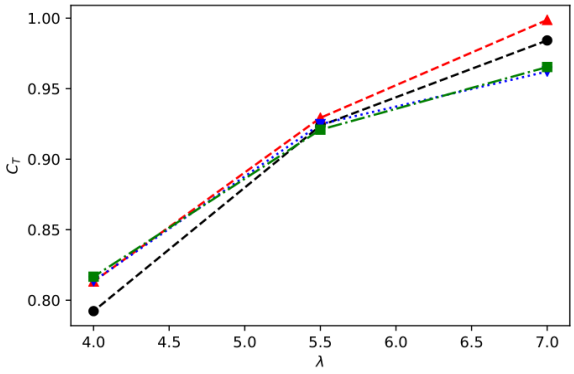

(b) Thrust coefficients

Fig. 10. Integrated quantities: Power coefficients C_P(a) and thrust coefficients C_T (b) as a function of tip-speed ratio for the four deformation cases.

$$C_T = \frac{T}{1/2\rho\pi R^2 V_\infty Y^2} \tag{4}$$

$$C_P = \frac{Q\omega}{1/2\rho\pi R^2 V_\infty Y^3} \tag{5}$$

from where T is the overall thrust on the rotor, Q the torque, ω the rotational speed, ρ the fluid density, R the turbine radius and V_∞ the undisturbed flow velocity.

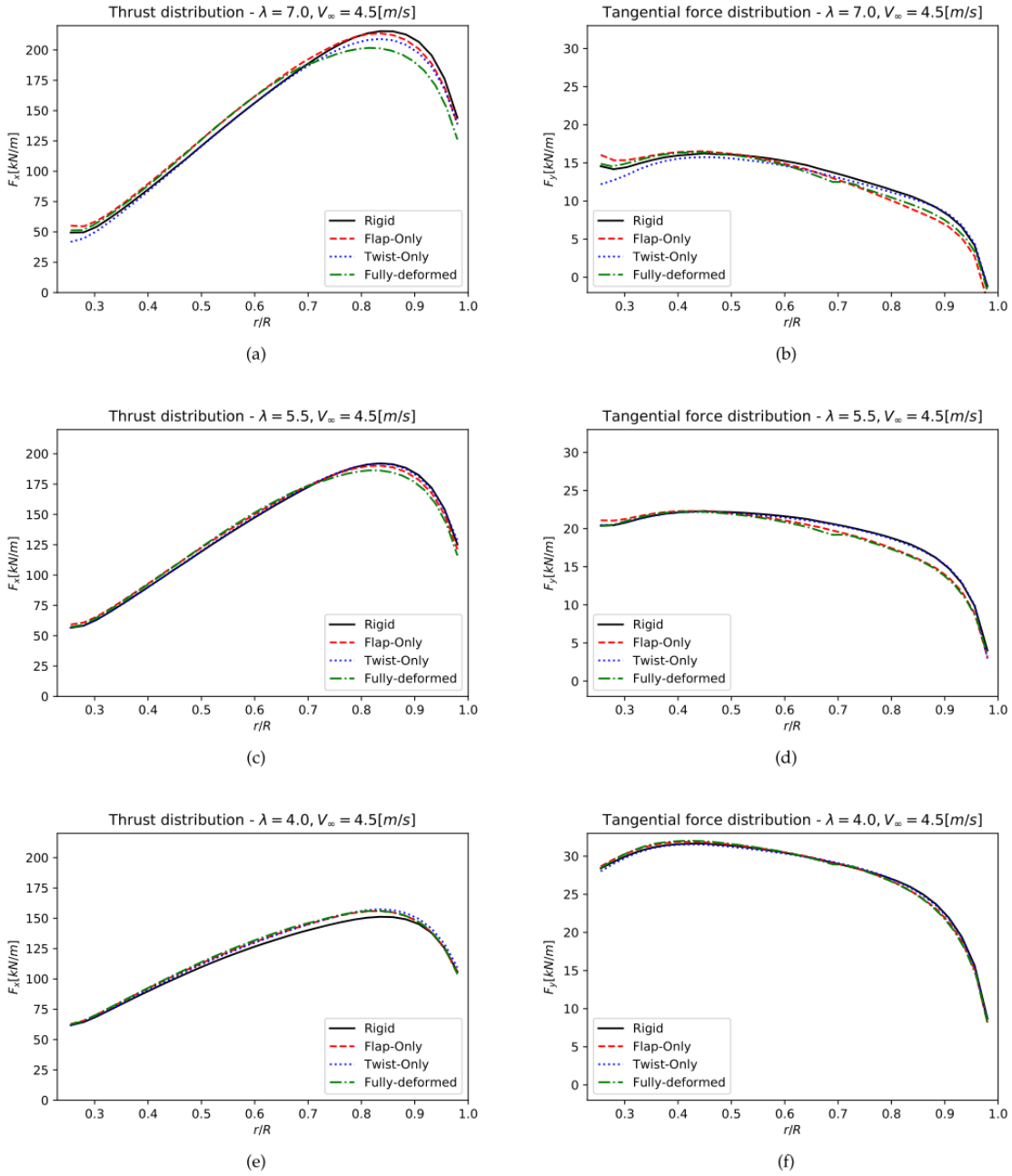

Fig. 11. Forces distribution at different tip-speed ratios for the different blade deformation cases.

The corresponding plots for the different deformation cases as a function of tip-speed ratio can be seen in Figs. 10 (a) and (b) for C_P and C_T, respectively.

F. Spanwise distribution of thrust and tangential force

The thrust and tangential forces, defined as a function of the radial position r, are extracted from the CFD by integrating the pressures over a series of slices at several radial locations. Then, the local thrust and tangential forces $\vec{F} = [F_X, F_Y]$ are obtained by integrating the pressures and shear forces over C, the blade transverse section at r, according to the following equation, from where p is the pressure, $\hat{n}$ is the unitary normal vector, and $\vec{S}$ the wall shear force.

$$\vec{F}(r) = \oint (p \cdot \hat{n} + \vec{S}) dC \tag{6}$$

The force distributions are plotted in Fig.11.

G. Induction factors

The axial induction factors are obtained by calculating the average of the flow-wise velocity component over a finite number of annular sections according to eq. 7, where V is the local flow velocity in the turbine plane, V_∞ the undisturbed flow velocity and a the axial induction factor.

$$V = V_\infty (1 - a) \tag{7}$$

This concept comes from the actuator-disc theory, where the rotor is considered as a flat surface where a

pressure discontinuity in the flow occurs. However, as the turbine in the CFD model has a non-zero thickness in the flow direction, the velocities at the turbine are estimated by averaging the velocities of the annular sections both upstream and downstream. These are located at a distance of $1.0c$ from the $0.25c$ line in the flow-wise direction, thus maintaining the nondimensional distance to the foil sections constant with radius.

The spanwise variation in the axial induction factors for the three tip-speed ratios and the different deformation cases are displayed in the Figs. 12 (a) to (c).

VI. Discussion

H. Spanwise force distribution

From the results, it can be seen that the deformations cause small hydrodynamic effects relative to the rigid blade at the lower two tip-speed ratios (5.5 and 4.0) but are more significant at the higher end when $\lambda = 7.0$. This is because the biggest deformations occur at this operational condition.

In the case of the thrust forces, it is possible to identify two regions within the blade: the inboard sections, where the flapwise-only and fully-deformed cases see an increase in thrust, and the outer region where, at the two higher TSRs, there is some degree of load alleviation.

All deformation components tend to be smaller on the inboard sections, indicating that spanwise variations in flow may be significant and that the traditional assumption of annular independence in BEM theory may not be appropriate in such cases.

We seek to evaluate whether the flapwise, edgewise and twistwise hydrodynamic effects are linearly related. In that sense, if we assume the force distribution on the fully-deformed case to be a superposition of the flapwise-only and twist-only components over the rigid design, as shown in Eq. 8, where F^i is a force component for the different deformation cases as a function of the radial position r, it's then possible to obtain the results plotted in the Fig. 11.

$$F(r) = F^{Rig} + (F^{Flap} - F^{Rig}) + (F^{Twist} - F^{Rig}) \quad (8)$$

Limiting this analysis to the $\lambda = 7.0$ case, where the fluid-structure interaction effects tend to be larger in magnitude, it can be seen from the Fig. 13 (a) that the superposition assumption for thrust seems particularly suitable for the inboard sections of the blade, being able to reproduce the thrust increment in that region quite accurately thanks to the positive and negative contributions of the flapwise-only and twist-only components.

A similar effect is seen in the tip-region, where the thrust forces seem to be modelled well but with a smaller accuracy than in the inboard sections, probably caused by non-linear three-dimensional flow effects.

In terms of the tangential forces, it can be seen that, after adding up the different components to the undeformed case, the prediction seems to be relatively accurate when compared to the fully-deformed case in the whole blade. Nonetheless, and this applies to both the trust and tangential forces, being the differences between cases very small, this analysis must be taken just as preliminary and further studies are required to generalize such an approach in a way that could be used within engineering design tools.

I. Power and thrust coefficients

As seen in the previous section, the variations in terms of the forces tend to be relatively small for the analysed rotor and especially at low tip-speed ratios, which clearly explains why the variability on the power and thrust coefficients is limited (Figs. 13).

From the plots it can be seen that the deformations act reducing the power that can be extracted from the flow, operating at a sub-optimal condition. It is worth noticing how for the flapwise-only case, an increased thrust for the three different tip-speed ratios, driven by a higher trust in the inboard sections, is seen.

Another interesting insight is the thrust of the twist-only case, where there is an inflection between $\lambda = 4.0$ and 7.0 with respect to the rigid case. On the left side of the curve, C_T is higher than the undeformed case, whereas it's very similar at $\lambda = 5.5$ and it shifts to be smaller at the end of the TSR range. This is clearly associated to the twist distributions, displayed in Fig. 6 (c), as the angular deformations act in different directions for the different cases.

Furthermore, this can be explained by the vectorial decomposition of the thrust (C_X) and tangential (C_Y) force coefficients, shown in eqs. 9 and 10, expressed as functions of the angle of attack α, and ϕ the inflow angle, from where C_L and C_D are the two-dimensional lift and drag coefficients.

$$C_X = C_L(\alpha)cos\phi + C_D(\alpha)sin\phi \quad (9)$$

$$C_Y = C_L sin\phi - C_D(\alpha)cos\phi \quad (10)$$

For the thrust analysis (eq. 9), it is clear that the problem is dominated by the lift coefficient C_L, being approximately linear in the attached-flow regime at which the rotor should normally operate. For the whole TSR range and the provided angular deformations, $cos\phi$ will remain almost invariant and close to one, while the second term $C_D(\alpha)sin\phi$ will be small compared to the first. Thus, a higher angle of attack at a low λ, caused by the corresponding angular deflection on the twist-only case, will imply a higher lift and, thus, a higher thrust, whereas the opposite will occur for the higher end of the curve when $\lambda = 7.0$, as the deformations would act reducing the angle of attack (See Fig 6.c).

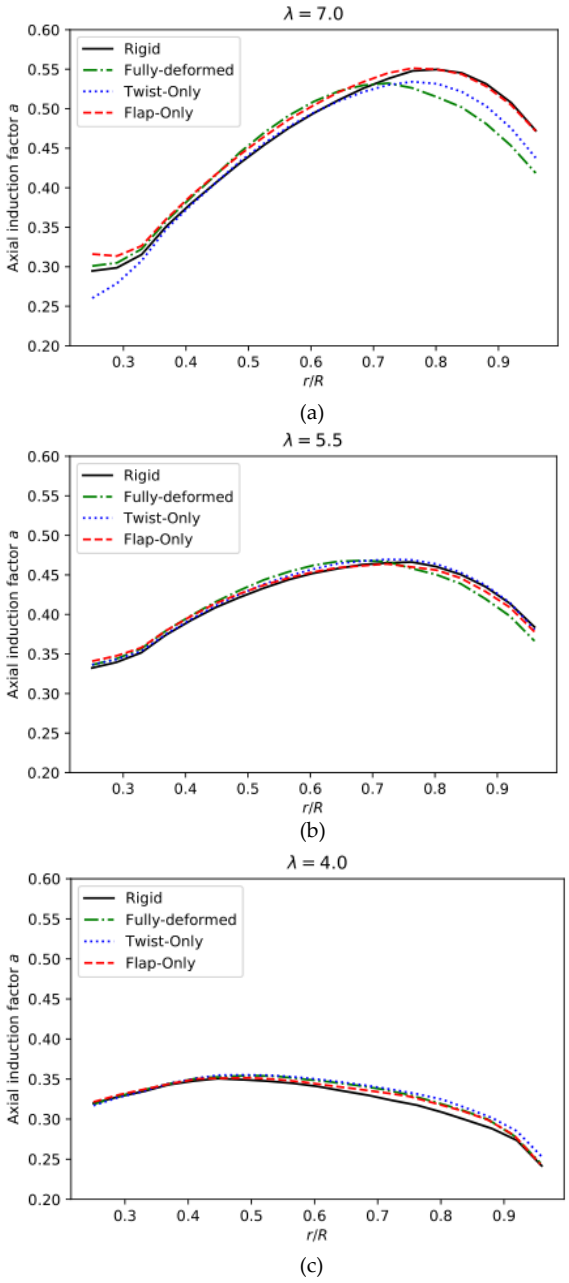

Fig. 12. Axial induction factors $a = 1 - V/V_\infty$ for the tip-speed ratios of: a) 7.0; b) 5.5; and c) 4.0.

However, the same is not seen on the power coefficient curve. This is in part associated to the tangential force C_Y, which is not dominated purely by C_L as it was in the thrust case, but it's also influenced by the trigonometric relationships and the drag term as well. In particular, for small angles, $sin\phi \approx \phi$ will influence the first term behaviour while remaining a small number, whereas the second term in the equation will act counteracting the first one. In addition, the inflow angle will be altered as well. Finally, it is worth noticing that the power seems also to be dominated by the action of the flapwise deformation, and more research is required to understand those effects.

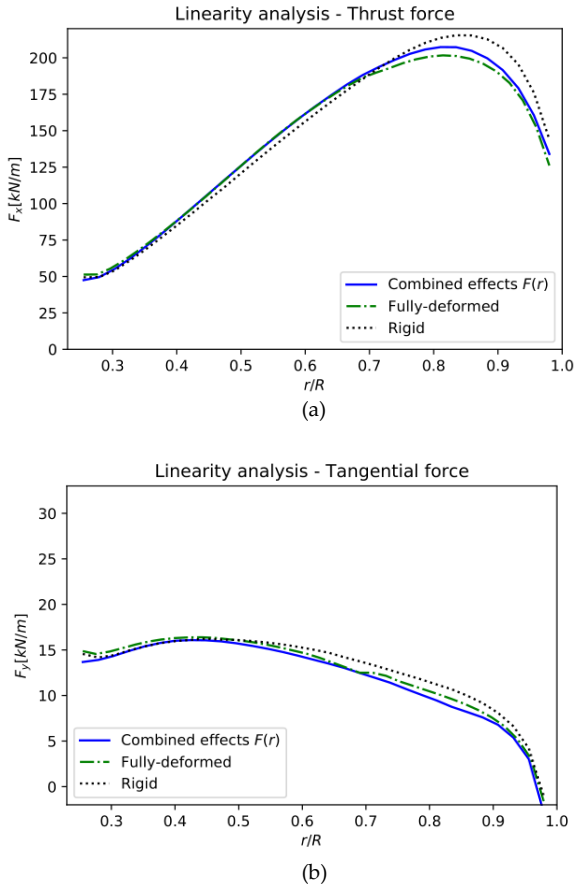

Fig. 13. Linear superposition analysis of the different deformation components for the thrust (a) and for the tangential (b) forces at a tip-speed ratio of 7.0. Three cases are presented: The rigid blade, the fully-deformed, and the combined effects $F(r)$ according to eq. 8.

VII. CONCLUSION

The present study presented an initial approach to de-couple the different deformation mechanisms seen in hydrokinetic turbines in a way that could make easier to include them as part of engineering models, and in that sense, to use them as a part of a design process to achieve more reliable and cost-effective rotors.

It is clear from this work that the different deformation mechanisms of a turbine are capable of influencing it's hydrodynamic performance. The results presented herein are encouraging as they also demonstrate that both the flapwise and the twist deformations have hydrodynamic effects, both of similar magnitude at least for the analysed case. In that regard, it seems not advisable to include just one of them in models while neglecting the other.

Another remarkable result from this work is the almost linear decomposition of the forces over the blade, showing that the de-coupling of the mechanisms could be a viable approach to model the phenomena. However, care must be placed here as, even considering that the simulations were carefully prepared, the variations are of reduced magnitude and the number of analysed cases limited, for which it's impossible to generalise from the results seen in this paper.

The biggest challenge in the close term is to accurately model the hyrodynamics of the flapwise component. This deformation shows effects that cannot be explained by simple vectorial decomposition, and the results presented in this paper suggest that the radial independence principle employed on the BEM theory would not remain valid. This can be seen both from the forces and induction factors presented herein, as effects can be observed even in regions of the blade that are not significantly affected by the rotor deflections.

Being able to model the flapwise effects would allow to develop reliable and accurate hydroelastic models that could be employed within design tools. Nonetheless, further studies are required to support this and to thoroughly describe the physics of the problem.

VIII. FUTURE WORK

The future steps in this research project are associated to obtain a deeper understanding of the physics of the different hydrodynamic effects of the deformation mechanisms. This involves developing the theoretical basis and tools to quantify flow effects such as changes in the angles of attack and induction factors as functions of the radial positions.

Once that understanding has been developed, it is necessary to analyse whether the deformations could be used as a viable passive control method for rotor control, capable of replacing complex pitching mechanisms, with the goal of increasing the reliability of tidal turbines and eliminating the costs associated with installing and operating complex immersed mechanisms.

If the passive control methods are proven to be a viable option, then the development of lower order methods that could be employed in engineering design and optimisation, such as the one developed in [17] but including all the physics of the problem, is going to be a priority.

ACKNOWLEDGEMENT

The authors would like to acknowledge the use of the University of Oxford Advanced Research Computing (ARC) facility in carrying out this work. http://dx.doi.org/10.5281/zenodo.22558

REFERENCES

[1] T. Burton, N. Jenkins, D. Sharpe, and E. Bossanyi, Wind energy handbook. John Wiley & Sons, 2011.

[2] J. Locke, U. Valencia, and K. Ishikawa, "Design studies for twist-coupled wind turbine blades," in ASME 2003 *Wind Energy Symposium*. American Society of Mechanical Engineers, 2003, pp. 324–331.

[3] R. Nicholls-Lee, S. Turnock, and S. Boyd, "A method for analysing fluid structure interactions on a horizontal axis tidal turbine," *EWTEC 2011 Proceedings*, 2011

[4] D. M. Grogan, S. B. Leen, C. R. Kennedy, and C. M Ó Brádaigh "Design of composite tidal turbine blades," *Renewable Energy*, vol. 57, pp. 151–162, 2013.

[5] R. Rafiee, M. Tahani, and M. Moradi, "Simulation of aeroelastic behavior in a composite wind turbine blade," *Journal of Wind Engineering and Industrial Aerodynamics*, vol.151, pp.60–69, 2016.

[6] G. S. Bir, M. J. Lawson, and Y. Li, "Structural Design of a Horizontal-Axis Tidal Current Turbine Composite Blade," *Volume 5: Ocean Space Utilization; Ocean Renewable Energy*, pp. 797–808, 2011.

[7] L. Wang, R. Quant, and A. Kolios, "Fluid structure interaction modelling of horizontal-axis wind turbine blades based on CFD and FEA," *Journal of Wind Engineering and Industrial Aerodynamics*, vol. 158, pp. 11–25, 2016.

[8] R. Nicholls-Lee, "Adaptive Composite Blades for Horizontal Axis Tidal Turbines," Doctoral thesis, University of Southampton, 2011.

[9] R. E. Murray, T. Nevalainen, K. Gracie-Orr, D. A. Doman, M. J. Pegg, and C. M. Johnstone, "Passively adaptive tidal turbine blades: Design tool development and initial verification," *International Journal of Marine Energy*, vol. 14, pp. 101–124, 2016.

[10] R. E. Murray, S. Ordonez-Sanchez, K. E. Porter, D. A. Doman, M. J. Pegg, and C. M. Johnstone, "Towing tank testing of passively adaptive composite tidal turbine blades and comparison to design tool," *Renewable Energy*, vol. 116, pp. 202–214, 2018.

[11] Y. Bazilevs, M.-C. Hsu, J. Kiendl, R. W¨uchner, and K.-U. Bletzinger, "3D simulation of wind turbine rotors at full scale. Part II: Fluid-structure interaction modeling with composite blades," *International Journal for Numerical Methods in Fluids*, pp. 65:236– 254, 2011.

[12] L. Wang, X. Liu, N. Renevier, M. Stables, and G. M. Hall, "Nonlinear aeroelastic modelling for wind turbine blades based on blade element momentum theory and geometrically exact beam theory," *Energy*, vol. 76, pp. 487–501, 2014.

[13] J. Schluntz and R. Willden, "The effect of blockage on tidal turbine rotor design and performance," *Renewable Energy*, vol. 81, pp. 432–441, 2015.

[14] A. Wimshurst and R. Willden, "Computational analysis of blockage designed tidal turbine rotors," *Progress in Renewable Energies Offshore - Proceedings of 2nd International Conference on Renewable Energies Offshore, RENEW 2016*, Emec, pp. 587– 597, 2016.

[15] S. A. Ning, "A simple solution method for the blade element momentum equations with guaranteed convergence," *Wind Energy*, vol. 17, no. 9, pp. 1327–1345, 2014.

[16] M. L. Buhl, "A New Empirical Relationship between Thrust Coefficient and Induction Factor for the Turbulent Windmill State A New Empirical Relationship between Thrust Coefficient and Induction Factor for the Turbulent Windmill State" *Technical Report NREL/TP-500-36834*, August, 2005.

[17] F. Zilic de Arcos, R. Willden, and C. Vogel, "Hydroelastic modelling of composite tidal turbine blades," in *RENEW 2018*, Lisbon, 2018.

[18] P. Fuglsang, K. S. Dahl, and I. Antoniou, "Wind tunnel tests of the Risø-A1-18, Risø-A1-21 and Risø-A1-24 airfoils". *Risø National Laboratory*, 1999.

[19] A. Fluent, "Ansys fluent theory guide 19.0," *ANSYS, Canonsburg*, PA, 2018.

[20] F. R. Menter, "Two-equation eddy-viscosity turbulence models for engineering applications," *AIAA journal*, vol. 32, no. 8, pp. 1598–1605, 1994.

[21] F. R. Menter, M. Kuntz, and R. Langtry, "Ten Years of Industrial Experience with the SST Turbulence Model," *Turbulence Heat and Mass Transfer 4*, vol. 4, pp. 625–632, 2003.

[22] C. Garrett and P. Cummins, "The efficiency of a turbine in a tidal channel," *Journal of Fluid Mechanics*, vol. 588, pp. 243–251, 2007.

[23] J. Luo and A. Gosman, "Prediction of impeller-induced flow in mixing vessels using multiple frames of reference." INSTITUTE OF CHEMICAL ENGINEERS SYMPOSIUM SERIES, 1994.